

Schell, Juliana; Zyabkin, Dmitry; Bharuth-Ram, Krish; Gonçalves, João N.;
Díaz-Guerra, Carlos; Gunnlaugsson, Haraldur P.; Martín-Luengo, Aitana Tarazaga;
Schaaf, Peter; Bonanni, Alberta; Masenda, Hilary; Dang, Thien Thanh;
Mølholt, Torben E.; Ólafsson, Sveinn; Unzueta, Iraultza; Mantovan, Roberto;
Johnston, Karl; Gíslason, Hafliði Pétur; Krastev, Petko B.; Naidoo, Deena;
Qi, Bingcui

**Anisotropy of the electric field gradient in two-dimensional α -MoO₃
investigated by ⁵⁷Mn(⁵⁷Fe) emission Mössbauer spectroscopy**















Original published in: Crystals. - Basel : MDPI. - 12 (2022), 7, p. 1-13.
Original published: 2022-07-04
ISSN: 2073-4352
DOI: [10.3390/cryst12070942](https://doi.org/10.3390/cryst12070942)
[Visited: 2022-09-16]



This work is licensed under a [Creative Commons Attribution 4.0 International license](https://creativecommons.org/licenses/by/4.0/). To view a copy of this license, visit <https://creativecommons.org/licenses/by/4.0/>

Article

Anisotropy of the Electric Field Gradient in Two-Dimensional α -MoO₃ Investigated by ⁵⁷Mn(⁵⁷Fe) Emission Mössbauer Spectroscopy

Juliana Schell ^{1,2,*}, Dmitry Zybakin ³, Krish Bharuth-Ram ⁴, João N. Gonçalves ⁵, Carlos Díaz-Guerra ⁶, Haraldur P. Gunnlaugsson ⁷, Aitana Tarazaga Martín-Luengo ⁸, Peter Schaaf ³, Alberta Bonanni ⁸, Hilary Masenda ^{9,10}, Thien Thanh Dang ², Torben E. Mølholt ¹, Sveinn Ólafsson ⁷, Iraultza Unzueta ¹¹, Roberto Mantovan ¹², Karl Johnston ¹, Hafliði P. Gíslason ⁷, Petko B. Krastev ¹³, Deena Naidoo ⁹ and Bingcui Qi ⁷

- ¹ European Organization for Nuclear Research (CERN), 1211 Geneva, Switzerland; torbenmolholt@gmail.com (T.E.M.); karl.johnston@cern.ch (K.J.)
 - ² Institute for Materials Science and Center for Nanointegration Duisburg-Essen (CENIDE), University of Duisburg-Essen, 45141 Essen, Germany; thien.dang@uni-due.de
 - ³ Chair Materials for Electrical Engineering and Electronics, Institute of Materials Science and Engineering, Institute of Micro and Nanotechnologies MacroNano[®], TU Ilmenau, Gustav-Kirchhoff-Strasse 5, 98693 Ilmenau, Germany; dmitry.zybakin@cern.ch (D.Z.); peter.schaaf@tu-ilmenau.de (P.S.)
 - ⁴ School of Chemistry and Physics, University of KwaZulu-Natal, Durban 4001, South Africa; kbharuthram@gmail.com
 - ⁵ CICECO—Aveiro Institute of Materials and Departamento de Física, Universidade de Aveiro, 3810-193 Aveiro, Portugal; joaonsg@ua.pt
 - ⁶ Departamento Física de Materiales, Facultad de Ciencias Físicas, Universidad Complutense de Madrid, 28040 Madrid, Spain; cdiazgue@fis.ucm.es
 - ⁷ Science Institute, University of Iceland, Dunhaga 3, 107 Reykjavík, Iceland; hpgunnlaugsson@gmail.com (H.P.G.); sveinol@hi.is (S.Ó.); hafliði@hi.is (H.P.G.); bingcui@hi.is (B.Q.)
 - ⁸ Quantum Materials Group, Institute for Semiconductor and Solid State Physics, Johannes Kepler University, Altenbergerstr. 69, 4040 Linz, Austria; aitana555@gmail.com (A.T.M.-L.); alberta.bonanni@jku.at (A.B.)
 - ⁹ School of Physics, University of the Witwatersrand, Johannesburg 2050, South Africa; hilary.masenda@wits.ac.za (H.M.); deena.naidoo@wits.ac.za (D.N.)
 - ¹⁰ Faculty of Physics and Materials Sciences Center, Philipps-Universität Marburg, 35032 Marburg, Germany
 - ¹¹ Department of Applied Mathematics, University of the Basque Country (UPV/EHU), Torres Quevedo Ingeniaria Plaza 1, 48013 Bilbao, Spain; iraultza.unzueta@gmail.com
 - ¹² CNR-IMM, Unit of Agrate Brianza, Via Olivetti 2, 20864 Agrate Brianza (MB), Italy; roberto.mantovan@mdm.imm.cnr.it
 - ¹³ Institute for Nuclear Research and Nuclear Energy, Bulgarian Academy of Sciences, 72 Tsarigradsko Chaussee Boulevard, 1784 Sofia, Bulgaria; pkrastev2002@abv.bg
- * Correspondence: juliana.schell@cern.ch



Citation: Schell, J.; Zybakin, D.; Bharuth-Ram, K.; Gonçalves, J.N.; Díaz-Guerra, C.; Gunnlaugsson, H.P.; Martín-Luengo, A.T.; Schaaf, P.; Bonanni, A.; Masenda, H.; et al. Anisotropy of the Electric Field Gradient in Two-Dimensional α -MoO₃ Investigated by ⁵⁷Mn(⁵⁷Fe) Emission Mössbauer Spectroscopy. *Crystals* **2022**, *12*, 942. <https://doi.org/10.3390/cryst12070942>

Academic Editor: Igor Neri

Received: 1 June 2022

Accepted: 29 June 2022

Published: 4 July 2022

Publisher's Note: MDPI stays neutral with regard to jurisdictional claims in published maps and institutional affiliations.



Copyright: © 2022 by the authors. Licensee MDPI, Basel, Switzerland. This article is an open access article distributed under the terms and conditions of the Creative Commons Attribution (CC BY) license (<https://creativecommons.org/licenses/by/4.0/>).

Abstract: Van der Waals α -MoO₃ samples offer a wide range of attractive catalytic, electronic, and optical properties. We present herein an emission Mössbauer spectroscopy (eMS) study of the electric-field gradient (EFG) anisotropy in crystalline free-standing α -MoO₃ samples. Although α -MoO₃ is a two-dimensional (2D) material, scanning electron microscopy shows that the crystals are 0.5–5- μ m thick. The combination of X-ray diffraction and micro-Raman spectroscopy, performed after sample preparation, provided evidence of the phase purity and crystal quality of the samples. The eMS measurements were conducted following the implantation of ⁵⁷Mn ($t_{1/2} = 1.5$ min), which decays to the ⁵⁷Fe, 14.4 keV Mössbauer state. The eMS spectra of the samples are dominated by a paramagnetic doublet (D1) with an angular dependence, pointing to the Fe²⁺ probe ions being in a crystalline environment. It is attributed to an asymmetric EFG at the eMS probe site originating from strong in-plane covalent bonds and weak out-of-plane van der Waals interactions in the 2D material. Moreover, a second broad component, D2, can be assigned to Fe³⁺ defects that are dynamically generated during the online measurements. The results are compared to ab initio simulations and are discussed in terms of the in-plane and out-of-plane interactions in the system.

Keywords: α -MoO₃; emission Mössbauer spectroscopy; two-dimensional (2D) material; ab initio simulations

1. Introduction

Two-dimensional (2D) inorganic materials, such as α -MoO₃, have attracted significant attention lately by virtue of their distinct properties and highly specific surface areas [1]. The room-temperature (RT)-stable orthorhombic α -MoO₃ phase is a wide-bandgap (2.8–3.2 eV) semiconductor of great practical interest mainly due to its anisotropic layered structure with weak interaction between (010) planes. Due to these structural characteristics, α -MoO₃ performs well in applications such as solar cells [1], catalysis [2], gas sensing [3], field emission [4], lithium-ion batteries [5], and photochromic devices [6]. In particular, α -MoO₃ films are used as an electrochromic layer in optical switches, electrochromic devices, and smart windows [7].

Oxygen vacancies play a key role in the physical properties of Mo oxides and their electrical conductivity by introducing gap states and influencing the optical bandgap. The oxygen-defect concentration is controlled by the oxygen partial pressure and preparation temperatures during synthesis, which in turn influences the crystal morphology. In this regard, thermal treatment under a low oxygen partial pressure, ion implantation, or ultraviolet (UV) irradiation of MoO₃ induces oxygen defects, leading to MoO_{3-x} [8]. Moreover, an appropriate combination of several Mo oxides or an adequate distribution of Mo ions with different oxidation states may lead to materials with emergent electronic and optical properties. For instance, MoO₃ is a transparent semiconductor, whereas MoO₂ is a metallic conductor. To gain deeper insight into these phenomena, a systematic investigation into the relationship between the stoichiometry and electronic structure over the range of oxidation states of MoO₃ and MoO_{3-x} is urgently required.

To tune the characteristics of α -MoO₃, doping with several cations (e.g., In cations) has been proposed [9]. Moreover, doped and undoped samples have been studied via conventional characterization methods. Strong and stable RT photoluminescence has been achieved in MoO₃ crystals doped with Er and Eu by ion implantation [10]. These results motivated our present study to further investigate the structural properties of samples via ion implantation. For instance, Pereira et al. implanted oxygen ions at RT to modify the electrical and structural properties of α -MoO₃ crystals [11]. The samples were also characterized after exposure to UV and proton-beam irradiation [12]. The creation of electron-hole pairs and the adsorption and desorption of oxygen molecules at the surface of the samples have been associated with variations in conductivity. The authors (Pereira et al.) further suggest that tuning the electrical properties by ion implantation offers possibilities for novel device designs.

The physics behind the multiple above-mentioned applications is linked to the material phenomenology, which includes defects such as oxygen vacancies, point defects, and impurity doping, all of which can be studied by Mössbauer spectroscopy (MS), as shown in earlier studies [13–15].

In an early ⁵⁷Fe MS study by Zhetbaev et al. on the formation kinetics of Mo oxides [13], a 99.5% Mo foil coated with a ⁵⁷Co isotope was subjected to different annealing atmospheres, both in hydrogen and in air. All measurements were performed at RT. The MoO₃ spectrum obtained after annealing at 700 °C presents two doublets. The authors present hyperfine parameters relative to the emission scale and relative to ⁵⁷Fe/Co in Cr metal. After adjusting for the reference scale [16] for α -Fe and changing the sign to represent a conventional isomer-shift scale, the one doublet has an isomer shift $\delta_{RT1} = 1.19$ mm/s with a quadrupole splitting $\Delta E_1 = 1.20$ mm/s while the second has $\delta_{RT2} = 0.21$ mm/s with $\Delta E_2 = 0.75$ mm/s, corresponding to the Fe²⁺ and Fe³⁺ states in a ratio of approximately 3:1. The authors also report that oxidation in air produces molybdenum with valences of 4⁺ and 6⁺, with other valence states making no significant contribution [13].

Effects of Fe Doping in MoO_x

Ab initio simulations of the effects of Fe doping of MoO_x indicate that Fe on substitutional Mo sites exhibits a compensating behavior, since Fe can act as a donor under p-type conditions and as an acceptor under n-type conditions [17,18].

Conventional characterization of Fe-doped MoO₂ films reveals resistivity minima and negative magnetoresistance below the resistive minima temperature [19]. This phenomenon is attributed to either weak localization or Kondo scattering of the conduction electrons from Fe impurities [19].

An appropriate amount of Fe doping can improve the gas-sensing properties of the system, notably at low operating temperatures [18]. The great advantage of presenting a stratified structure is that different dopants can be incorporated into the gaps between the layers in the crystal lattice, a mechanism that is essential for the electrochromic and catalytic applications of α -MoO₃ [10].

Motivated by the interesting properties arising from stoichiometry dependencies, we used ⁵⁷Fe emission Mössbauer spectroscopy (eMS) to study highly crystalline molybdenum trioxide lamellar samples with implanted ⁵⁷Mn. Particular attention was given to the influence of the incorporated Fe probe in different configurations in the α -MoO₃ system, with the results supported by ab initio simulations.

2. Materials and Methods

α -MoO₃ lamella single crystals were grown by sublimation with the growth conditions optimized following the methods described in a previous work [10]. Pure Mo powder was compacted under a compressive load to form disks, which were inserted into a quartz tube and annealed in air at 750 °C for 10 h in a horizontal tube furnace. Under these conditions, numerous high-quality α -MoO₃ lamella crystals were deposited on the cooler part of the internal wall of the quartz tube. Scanning electron microscopy (SEM) (Madrid, Spain), energy-dispersive X-ray spectroscopy (EDX-SEM), X-ray diffraction (XRD), and micro-Raman characterizations of the samples were performed at RT before implantation of the ⁵⁷Mn ions. The XRD measurements were carried out on a Philips X'Pert PRO diffractometer (Madrid, Spain) using Cu K α radiation. The micro-Raman measurements were carried out in a Horiba Jobin-Yvon LabRAM HR800 system (Madrid, Spain), in which the samples were excited by a 633 nm He-Ne laser on an Olympus BX41 confocal microscope with a 100 \times objective. The spectral resolution of the system used was approximately 1 cm⁻¹.

⁵⁷Fe eMS measurements [20,21] were performed at the ISOLDE-CERN facility [22,23], where the parent radioactive isotope was produced with 1.4 GeV proton-induced fission in a heated UC₂ target. Mass-separated ⁵⁷Mn ions were then implanted with an energy of 50 keV into the samples at RT. Emission Mössbauer spectra were recorded using a resonance detector equipped with a ⁵⁷Fe-enriched stainless-steel electrode mounted on a conventional drive system outside the implantation chamber at 60° relative to the sample normal. The implantation fluence was less than 2 \times 10¹¹ ⁵⁷Mn ions/cm², which is a dilute concentration [14,24]. SRIM simulations give an average implantation depth of the order of 30 nm [25]. Estimates of the sample volume that turns amorphous upon implantation were determined from angular-dependent studies in which the sample holder was rotated to acquire data at emission angles of 0°, 30°, and 60° (no rotation) relative to the sample normal (normal to the lamellar plane). Figure 1a illustrates the orientation of flakes mounted relative to the incident Mn beam, and Figure 1b provides a sketch of the top view of the implantation set-up used to identify the incident and emission angles involved.

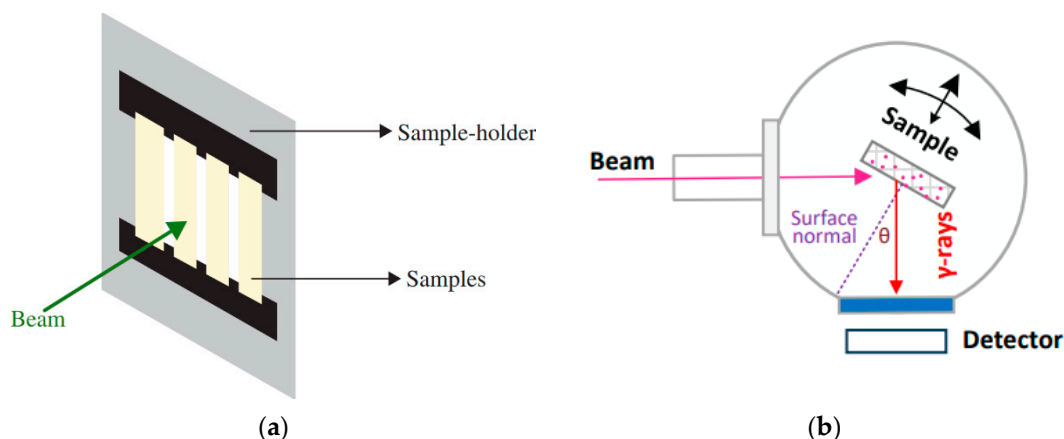


Figure 1. (a) Schematic view showing the orientation of the samples relative to the direction of the ^{57}Mn beam. (b) Top view of the experimental set-up indicating the γ -emission angle θ .

The ab initio simulations used the Vienna ab initio simulation package [26], with the projector augmented-wave method [27]. The electron configurations considered were 4p, 4d, and 5s for Mo; 3p, 3d, and 4s for Fe; and 2s and 2p for O. The Perdew–Burke–Ernzerhof generalized gradient approximation exchange–correlation approximation was used [28], with an additional U term of 4.38 eV at Mo d orbitals and 3 eV at Fe d orbitals to better describe these highly correlated states [29]. The plane waves were expanded with an energy cut-off of 520 eV, and a Γ -centered Monkhorst–Pack k-point grid of $1 \times 9 \times 9$ k points was used for the unit cell, with similar densities for supercells. The forces were minimized to less than $0.01 \text{ eV}/\text{\AA}$.

3. Results

Figure 2 shows the SEM results for a sample (lamellar crystals), with 400 and 200 μm scale bars. Although $\alpha\text{-MoO}_3$ is a 2D material, the crystals investigated herein were 0.5–5- μm thick. Widths typically exceed 300 μm , and lengths can reach 1 cm.

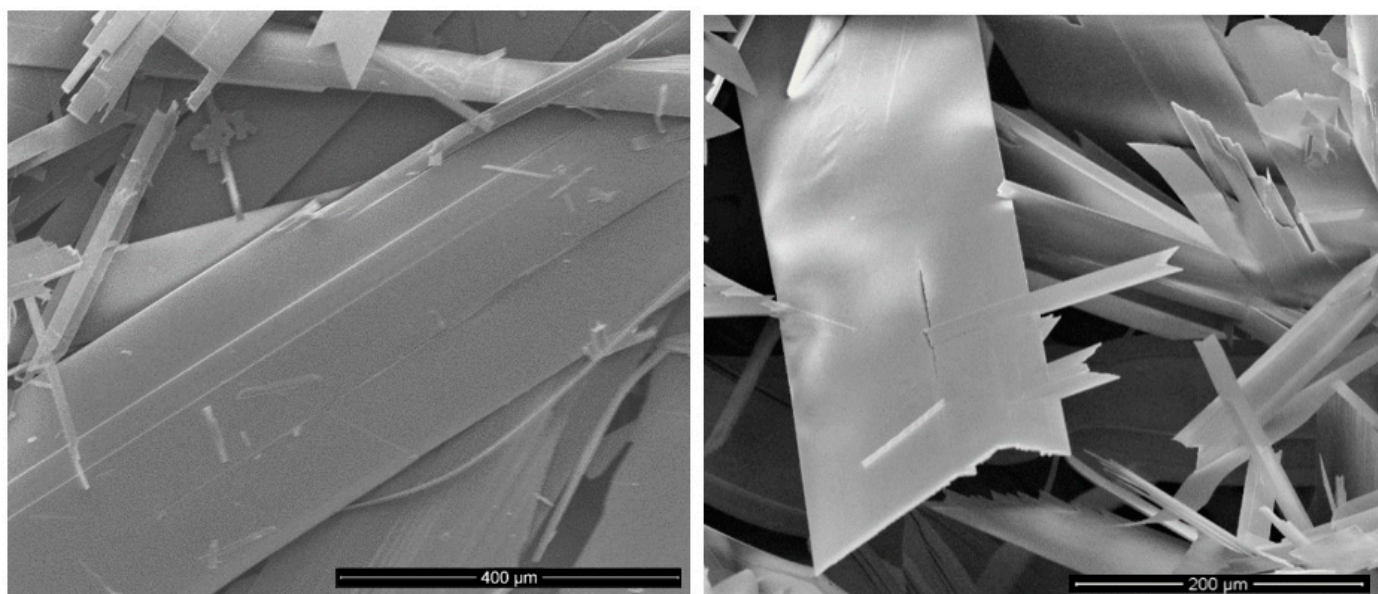


Figure 2. Room-temperature SEM images of samples taken before the implantation process.

The long-range and short-range structural information of the as-grown crystals was characterized by XRD and micro-Raman spectroscopy, respectively. Figure 3a shows the

chemical composition of the samples obtained via SEM-EDX microanalysis, which revealed no other elements but Mo and O, besides a weak C signal from the graphite tape used to stick the sample to the SEM sample holder. The as-grown α -MoO₃ crystals showed a characteristic layered structure. Based on the crystal morphology, a two-dimensional layer-by-layer mechanism has been proposed to account for the nucleation and growth of this kind of oxide crystals. In fact, from an energy perspective, planar growth rates along the axes of the crystal follow the sequence $\{001\} > \{100\} > \{010\}$. Hence, it is highly favorable for α -MoO₃ crystals to grow along the [1] direction with the largest exposed surface of $\{010\}$ facets [30], in agreement with our XRD patterns.

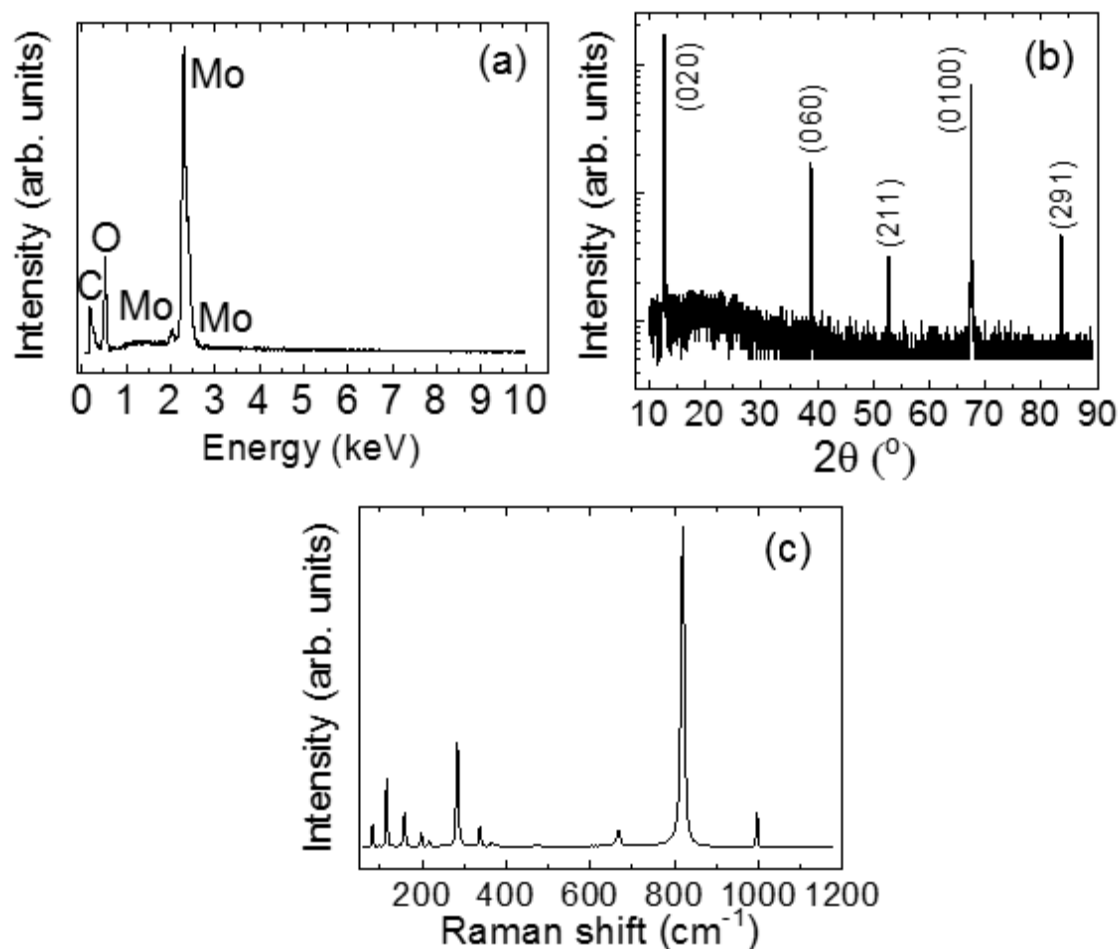


Figure 3. (a) SEM–EDX spectrum, (b) XRD pattern, and (c) Raman spectrum of the as-grown crystals.

Figure 3b shows an XRD pattern of the samples. The spectrum was plotted on a logarithmic scale to show the low-intensity diffraction maxima. All strong and sharp diffraction maxima can be indexed to orthorhombic α -MoO₃ (JCPDS 05-0508). A clear preferential $(0k0)$ orientation is apparent, consistent with the 2D structure and growth habits of this oxide [31,32]. No other phases are evident in our XRD measurements. The lattice parameters determined were $a = 13.878 \text{ \AA}$, $b = 3.696 \text{ \AA}$, and $c = 3.961$, in very good agreement with file JCPDS 05-0508.

Figure 3c presents a representative Raman spectrum of the as-grown crystals. All observed bands are unambiguously attributed to the orthorhombic α -MoO₃ phase [32,33]. Peaks appear to be centered at 996 (A_g , ν_{as} M=O stretch), 819 (A_g , ν_s M=O stretch), 667 (B_{2g} , B_{3g} , ν_{as} O–M–O stretch), 472 (A_g , ν_{as} O–M–O stretch and bend), 380 (B_{1g} , δ O–M–O scissor), 365 (A_{1g} , δ O–M–O scissor), 338 (A_g , B_{1g} , δ O–M–O bend), 283 (B_{2g} , δ O=M=O wagging), 217 (A_g , rotational rigid MoO₄ chain mode, R_c), 198 (B_{2g} , τ O=Mo=O twist),

158 (A_g/B_{1g} , translational rigid MoO_4 chain mode, T_b), 129 (B_{3g} , translational rigid MoO_4 chain mode, T_c), 116 (B_{2g} , translational rigid MoO_4 chain mode, T_c), 99 (B_{2g} , translational rigid MoO_4 chain mode, T_a), and 83 cm^{-1} (A_g , translational rigid MoO_4 chain mode, T_a).

The combination of XRD and Raman spectroscopy provides definitive evidence of the phase purity and crystal quality of the investigated material prior to the eMS measurements. Moreover, Raman measurements were carried out in a system equipped with a confocal microscope, which provided spatial resolution and allowed us to check that no differences were found, either in terms of the peak shifts or widths, between spectra measured for different crystals or at different spots of the same sample.

Figure 4 presents the eMS spectra obtained at 0° , 30° , and 60° . Overall, the spectra can be fit with a quadrupole-splitting distribution (D1) with parameters (Table 1) typical of ionic Fe^{2+} [13]. Complete fits to the data require a second component (D2) due to Fe^{3+} ions in unresolved local environments. D2 seems to have a peak intensity of approximately $v \sim -0.3 \text{ mm/s}$ and gives rise to intensities in the wings of the spectra, which is most likely due to Fe^{3+} showing slow paramagnetic relaxations, as reported for earlier eMS measurements on metal oxides [34,35]. The intensities of the two peaks of D1 clearly display angular dependence.

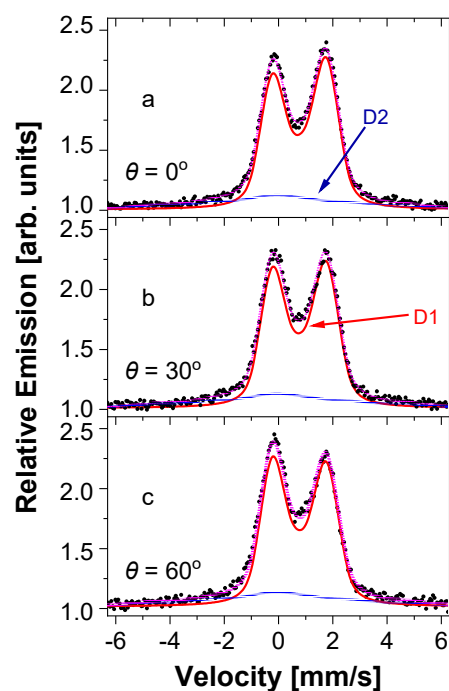


Figure 4. ^{57}Fe emission Mössbauer spectra of $\alpha\text{-MoO}_3$ lamella crystals obtained at room temperature after implantation of ^{57}Mn at (a) 0° , (b) 30° , and (c) 60° .

Table 1. Experimental hyperfine parameters obtained at RT for D1.

Emission Angle		0°
D1	δ (mm/s)	0.81(3)
	$\langle \Delta E_Q \rangle$ (mm/s)	1.81(6)
	Area (%)	69(6)

The Fe^{2+} component was assumed to have the same distribution in all spectra and was simulated using a probability function $P(\Delta E_Q)$, as shown in Figure 5, with three linear segments [36] in the Vinda analysis package [37]. The Fe^{2+} component has an isomer shift $\langle \delta_{RT} \rangle = 0.81(3) \text{ mm/s}$ and an average quadrupole splitting $\langle \Delta E_Q \rangle = 1.81(6) \text{ mm/s}$ with a

standard deviation of $\sigma(P(\Delta E_Q)) = 0.78(6)$ mm/s, meaning that the relative distribution [35] of the quadrupole splitting was $\sigma(P(\Delta E_Q))/\langle\Delta E_Q\rangle = 43(4)\%$. Such a high value would, under normal circumstances, be attributed to amorphous local surroundings, but the angular dependence suggests that the probe atoms sensed the crystalline structure of the host. In the final analysis, the area fraction of the Fe^{2+} component was set to be the same in all spectra: 69(6)%.

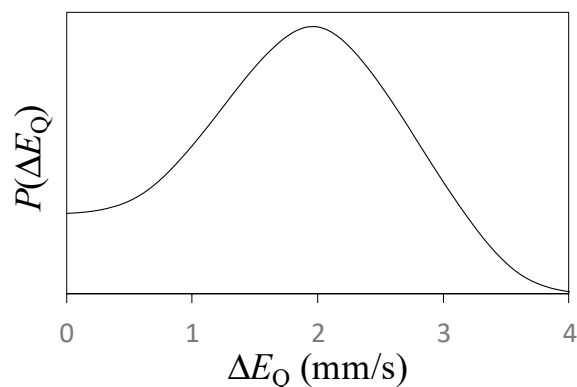


Figure 5. Quadrupole splitting distribution used to analyze the spectra in Figure 3 for spectral component D1. The linear segment distribution has been folded with the experimental line broadening.

Due to the underlying Fe^{3+} component (D2), it was not possible to determine the area ratio of the legs of the two emission peaks of the doublets in a free fitting, so restrictions had to be introduced. For D1, the ratio of the spectral area of the left emission peak (A_l) to that of the right emission peak (A_r) is expressed as [38]:

$$\frac{A_l}{A_r} = Q(f(\theta) - 1) + 1, \quad (1)$$

with:

$$f(\theta) = \frac{3 + 3 \cos^2 \theta}{5 - 3 \cos^2 \theta}, \quad (2)$$

where Q is a ‘quality’ factor for the angular dependence ($Q = 1$ represents full angular dependence for the $V_{ZZ} \parallel$ sample normal, and $Q = 0$ represents the polycrystalline case). The $Q = 0.08(2)$ value obtained from the fit for D1 is a small but significant departure from the polycrystalline case. The hyperfine parameters of D1 determined from our analysis are listed in Table 1. The parameters do not show a significant difference with the emission angle.

A first simulation step was to optimize the structural parameters for a pure $\alpha\text{-MoO}_3$ unit cell, obtaining the lattice parameters $a = 14.43$ Å, $b = 3.76$ Å, and $c = 3.97$ Å, which are close to the values reported from the XRD measurements performed at room temperature: $a = 13.85$ Å, $b = 3.69$ Å, and $c = 3.96$ Å [39]. The lattice parameters determined from our XRD data were $a = 13.878$ Å, $b = 3.696$ Å, and $c = 3.961$ Å and allow a more reasonable comparison with our experiments, which were performed at RT. We then constructed supercells from the optimized cell, $1 \times 3 \times 3$, with the substitution of one Fe for one of the equivalent Mo sites. The final structure was calculated by fully optimizing the atomic parameters while keeping the lattice parameters fixed to the values of the optimized state without Fe. We also considered the case where oxygen vacancies were close to the implanted Fe probe, and the case of having the Fe probe in the van der Waals gap (see Figures 6 and 7).

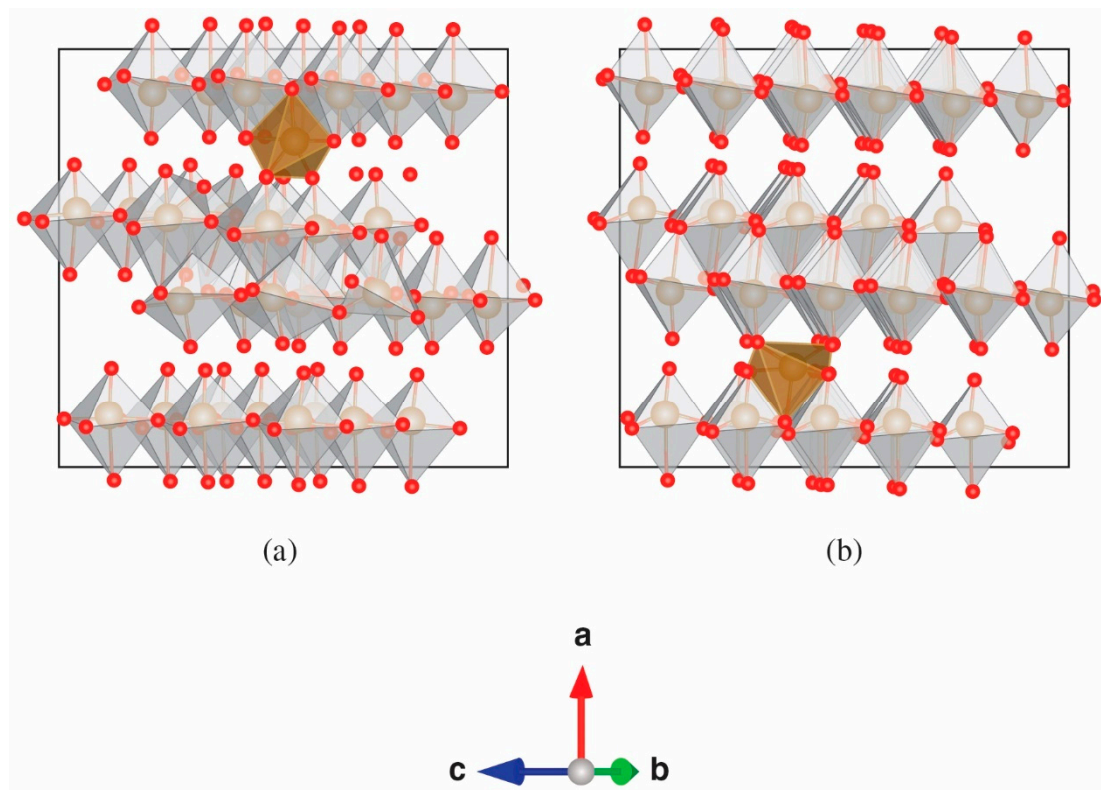


Figure 6. α - MoO_3 supercells with the Fe probe located in the van der Waals gap at (a) position 1 and (b) position 2. Drawings were produced by VESTA [40].

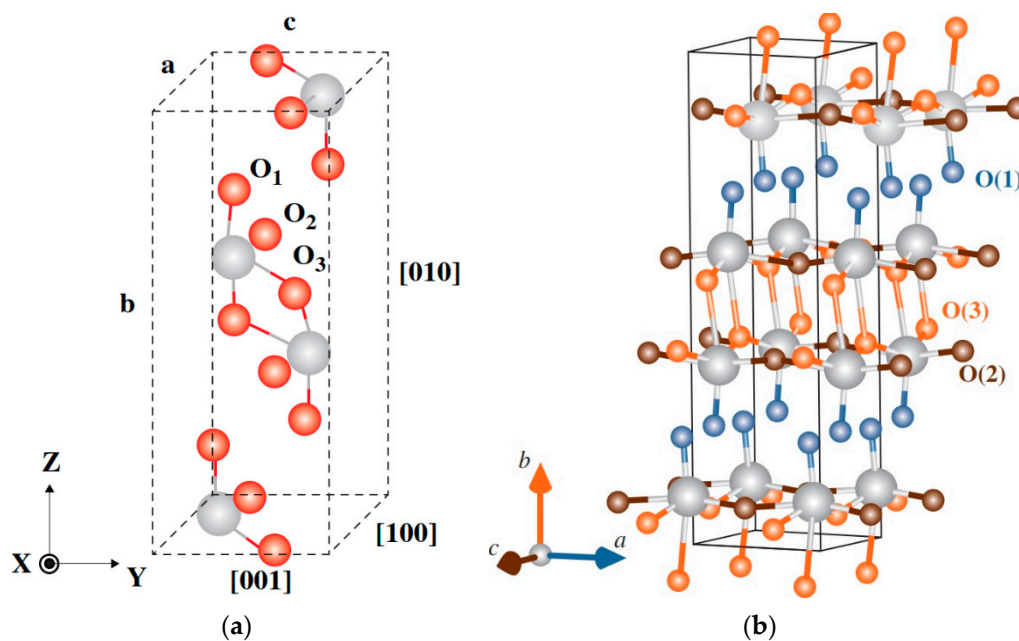


Figure 7. (a) Example of the local complexity of the α - MoO_3 unit cell (image produced by [41]). (b) Schematic of three non-equivalent O positions labeled with different colors (image produced by [17]). Large spheres represent Mo atoms while smaller spheres represent O atoms.

After relaxation, for the Fe probe located in the van der Waals gap, we obtained two positions between layers (see Figure 6), with one of slightly greater stability. We, therefore, calculated three additional configurations considering the subtraction of one, two, and

three electrons. Note that reducing the number of electrons in the calculation produced large changes in the electric-field gradient (EFG) in this case.

For oxygen vacancies close to the implanted Fe probe, all possible combinations of nearest-neighbor O vacancies were evaluated, where O(1), O(2), and O(3) denote singly, 2-fold, and 3-fold coordinated oxygen sites, respectively (see Figure 7). The results are shown in Table 2. The EFG can be converted to the quadrupole splitting using Equations (3) and (4) [42,43] and using $Q(^{57}\text{Fe}) = 0.17b$ [43], $I_e = 3/2$, $E_0 = 14.4$ keV for the ^{57}Fe resonant transition:

$$\Delta E_Q = 6 \left| A_Q \right| \sqrt{1 + \eta^2/3}, \quad (3)$$

$$A_Q = ecQV_{zz}/[4I_e(2I_e - 1)E_0]. \quad (4)$$

Table 2. Results for the calculation in $1 \times 3 \times 3$ supercells for the Fe probe in different configurations. Calculated V_{zz} , asymmetry parameter η , electric quadrupole splitting ΔE_Q , and total energy per formula unit (Fe/Mo atoms, there are 36 formula units) relative to the most stable state.

Fe Configuration	V_{zz} (10^{21} V/m ²)	η	ΔE_Q (mm/s)	Energy (meV/f.u.)
Substitutional to Mo	2.83	0.30	0.51	–
Substitutional to Mo with O(1) vacancy	10.18	0.00	1.81	0
Substitutional to Mo with O(2) vacancies	–7.94	0.15	1.41	39
Substitutional to Mo with O(3) vacancy	–3.90	0.40	0.71	96

The total energies obtained were compared with the cases with the same numbers of atoms so that only the atomic positions changed, making for a direct comparison. Energies for cases with one vacancy were compared with each other to find the most stable case. O(1) was the most stable vacancy.

The case with the O(1) vacancy is not only the most stable of those with one oxygen vacancy but also the case with the calculated quadrupole splitting closest to the average experimental value (experimental $\langle \Delta E_Q \rangle = 1.81(6)$ mm/s and calculated $\Delta = 1.81$ mm/s), further suggesting that this was the most likely arrangement in the experiments. In general, ab initio simulations are performed for 0 K, and our measurements were carried out at RT. It is rare to find ab initio simulations of EFGs for higher temperatures, since the commonly used density functional theory is valid strictly only for 0 K. Consideration of the temperature would require, for example, ab initio molecular dynamics for accurate interpretation of the experimental results. As mentioned before, optimized RT α -MoO₃ lattice parameters were used here in all configurations, and then the internal parameters were relaxed by force optimization to a force limit below 1 mRy/Å. This procedure is considerably fast [44] and is different from molecular dynamics approaches [45].

4. Discussion

4.1. Local Environment 1 (D1)

For D1, the isomer shift $\langle \delta_{RT} \rangle = 0.81(3)$ mm/s and the average quadrupole splitting $\langle \Delta E_Q \rangle = 1.81$ mm/s. According to our simulations, the observed hyperfine interaction would correspond to Fe at substitutional Mo sites with one neighboring O(1) vacancy. Given the nature of metal oxides, the Mo–O bonding energy can be easily overcome by direct implantation damage, producing nearby vacancies [46]. It is important to emphasize that the density functional theory employed in this work is valid strictly for 0 K. Therefore, it is not possible to directly compare our experimental value with the simulated one. Consideration of the temperature would require, for example, ab initio molecular dynamics, which will be part of our future work. To the best of our knowledge, there is no temperature-

dependence study in the literature that can provide the EFG trend close to RT for this complex system.

In the results presented here, D1 has an angular dependency, as can be seen by the dependence of the intensity of the two emission peaks on the emission angle. The angular dependence for the quadrupole splitting distribution of our measurements is due to Fe^{2+} and not to Fe^{3+} .

4.2. Local Environment 2 (D2)

The more likely interpretation of this component is an unresolved Fe^{3+} component, showing slow paramagnetic relaxations [34,35,47]. During ion implantation, the formation of various defect types, such as numerous interstitials and vacancies, should be considered, especially in the case of the broad distribution arising from the doublet, which is characteristic of high-spin Fe^{3+} . The present results confirm that the angular dependence shows that the probe atoms are in a crystalline environment for component D1. However, it is difficult to state anything quantitative for D2. The data from [13] suggested the presence of a fast-relaxing Fe^{3+} component (doublet), which implies that the Fe^{3+} was not dilute in their sample. Since, in our case, we have a very diluted implantation regime [14,24], it is not possible to compare our data with those reported in [13].

5. Conclusions

The structural properties of high-crystalline-quality $\alpha\text{-MoO}_3$ lamellar samples were studied via ion implantation at RT through eMS experiments at ISOLDE-CERN, following implantation of ^{57}Mn ($t_{1/2} = 1.5$ min), which decays to the 14.4 keV Mössbauer state. The spectra were fit to two broadened doublets. The results with Fe^{2+} show evidence of the single crystallinity of the local environment through the angular dependence of the quadrupole interaction for D1. The obtained hyperfine parameters indicate that the asymmetric doublet has a typical isomer shift of high-spin Fe^{2+} , which is $\langle\delta_{RT}\rangle = 0.8(3)$ mm/s, and the average quadrupole splitting $\langle\Delta E_Q\rangle = 1.81(6)$ mm/s. The second component is characterized by high-spin Fe^{3+} . The large quadrupole splitting of Fe^{2+} is likely due to a relatively highly distorted configuration near the implanted probe ion. Different configurations for the Fe probe were considered for the ab initio simulations, including Fe at the substitutional Mo site with and without O vacancies. Additionally, simulations considering the Fe probe between layers were performed with different electronic arrangements. The case of Fe at the substitutional Mo site with one vacancy (O1) is not only the most stable configuration among those with one oxygen vacancy but is also the configuration with the calculated quadrupole splitting closest to the average experimental value. However, it is not possible to assign this configuration to the case detected in our experiments with perfect confidence.

The combination of SEM, XRD, and Raman spectroscopy provided evidence of the phase purity, morphology, and crystal quality of the investigated material prior to the eMS measurements.

Ion implantation is a widely used industrial process because it is very easy to reproduce, and the defects introduced in the system can be of technological advantage. In particular, the physical properties of an impurity in the $\alpha\text{-MoO}_3$ system depend predominantly on its lattice location. The site of implanted dopants can be determined via the performed eMS measurements combined with ab initio simulations. Therefore, the current study provides a better understanding of the physical properties of Mn/Fe impurities in the $\alpha\text{-MoO}_3$ system. The next step is to study the interplay between the thermal effects of post-implantation annealing and the lattice location of Fe and possible defects [48].

Author Contributions: J.S. wrote the manuscript and performed the online measurements; D.Z., K.B.-R., I.U., and T.T.D. assisted with the manuscript writing; J.N.G. performed the simulations; C.D.-G. was responsible for sample preparation and conventional characterization; D.Z., H.P.G. (Haraldur P. Gunnlaugsson), A.T.M.-L., and P.S. were responsible for data analysis; A.T.M.-L. and A.B. contributed to data interpretation; D.Z., I.U., H.P.G. (Haraldur P. Gunnlaugsson), A.T.M.-L., H.M., K.B.-R., T.E.M., S.Ó., R.M., K.J., H.P.G. (Haflíði P. Gíslason), P.B.K., D.N., and B.Q. were also responsible for the online measurements. All authors have read and agreed to the published version of the manuscript.

Funding: We acknowledge the financial support received from the Federal Ministry of Education and Research (BMBF) through grants 05K16PGA, 05K16SI1, and 05K19SI1 ‘eMIL’ and ‘eMMA’. We acknowledge the support of the European Union’s Horizon 2020 Framework research and innovation program under grant agreement no. 654002 (ENSAR2) given to the ISOLDE experiment IS611 ‘Study of molybdenum oxide by means of Perturbed Angular Correlations and Mössbauer spectroscopy’. We further acknowledge Koichi Momma and Fujio Izumi, the creators of VESTA Version 3, for providing the license under Copyright (C) 2006–2021, Koichi Momma, and Fujio Izumi. We thank the Ministry of Economy and Competitiveness Consolider—Ingenio Project CSD2009 0013 ‘IMAGINE’ Spain, and Banco Santander-UCM, project PR87/19-22613. We also acknowledge Österreichische Forschungsförderungsgesellschaft funded projects Competence Headquarters Program E2-Spattertech, Austria, Project: FFGP13222004 and the Austrian Science Fund (FWF), Project: P31423. We are grateful for the support from the Icelandic University Research Fund. K. Bharuth-Ram, H. Masenda, and D. Naidoo acknowledge support from the South African National Research Foundation and the Department of Science and Innovation within the SA-CERN programme. H. Masenda also acknowledges support from the Alexander von Humboldt (AvH) Foundation. I. Unzueta acknowledges the support of Ministry of Economy and Competitiveness (MINECO/FEDER) for grant N° RTI2018-094683-B-C55. J. N. Gonçalves acknowledges support from by CICECO-Aveiro Institute of Materials (POCI-01-0145-FEDER-007679)—FCT reference (UID/CTM/50011/2013).

Institutional Review Board Statement: Not applicable.

Informed Consent Statement: Not applicable.

Data Availability Statement: Data are available upon reasonable request.

Acknowledgments: We also acknowledge the support of all the technical teams at ISOLDE for their excellent work in delivering high-quality beams for emission Mössbauer measurements.

Conflicts of Interest: The authors declare no conflict of interest.

References

1. Giroto, C.; Voroshazi, E.; Cheyns, D.; Heremans, P.; Rand, B.P. Solution-processed MoO₃ thin films as a hole-injection layer for organic solar cells. *ACS Appl. Mater. Interfaces* **2011**, *3*, 3244–3247. [[CrossRef](#)] [[PubMed](#)]
2. Labanowska, M. EPR monitoring of redox processes in transition metal oxide catalysts. *Chem. Phys. Chem.* **2001**, *2*, 712–731. [[CrossRef](#)]
3. Comini, E.; Yubao, L.; Brando, Y.; Sberveglieri, G. Gas sensing properties of MoO₃ nanorods to CO and CH₃OH. *Chem. Phys. Lett.* **2005**, *407*, 368–371.
4. Zhou, J.; Xu, N.-S.; Deng, S.-Z.; Chen, J.; She, J.-C.; Wang, Z.L. Large-area nanowire arrays of molybdenum and molybdenum oxides: Synthesis and field emission properties. *Adv. Mater.* **2003**, *15*, 1835–1840. [[CrossRef](#)]
5. Hu, X.; Zhang, W.; Liu, X.; Mei, Y.; Huang, Y. Nanostructured Mo-based electrode materials for electrochemical energy storage. *Chem. Soc. Rev.* **2015**, *44*, 2376–2404. [[CrossRef](#)]
6. Yao, J.N.; Hashimoto, K.; Fujishima, A. Photochromism induced in an electrolytically pretreated MoO₃ thin film by visible light. *Nature* **1992**, *355*, 624–626. [[CrossRef](#)]
7. Madhuri, K.V.; Dixit, D. Study on structural and optical properties of thermally evaporated MoO₃ thin films. *Bull. Mater. Sci.* **2022**, *45*, 83. [[CrossRef](#)]
8. Huang, P.-R.; He, Y.; Cao, C.; Lu, Z.-H. Impact of lattice distortion and electron doping on α -MoO₃ electronic structure. *Sci. Rep.* **2014**, *4*, 7131. [[CrossRef](#)]
9. Chen, H.Y.; Su, H.-C.; Chen, C.-H.; Liu, K.-L.; Tsai, C.-M.; Yen, S.-J.; Yew, T.-R. Indium-doped molybdenum oxide as a new p-type transparent conductive oxide. *Mater. Chem.* **2011**, *21*, 5745–5752. [[CrossRef](#)]
10. Vila, M.; Díaz-Guerra, C.; Jerez, D.; Lorenz, K.; Piqueras, J.; Alves, E. Intense luminescence emission from rare-earth doped MoO₃ nanoplates and lamellar crystals for optoelectronic applications. *J. Phys. D Appl. Phys.* **2014**, *47*, 355105. [[CrossRef](#)]

11. Pereira, D.R.; Díaz-Guerra, C.; Peres, M.; Magalhaes, S.; Correia, J.G.; Marques, J.G.; Silva, A.G.; Alves, E.; Lorenz, K. Engineering strain and conductivity of MoO₃ by ion implantation. *Acta Mater.* **2019**, *169*, 15–27; Erratum in **2020**, *199*, 425–428. [[CrossRef](#)]
12. Pereira, D.R.; Peresa, M.; Alves, L.C.; Correia, J.G.; Díaz-Guerra, C.; Silva, A.G.; Alves, E.; Lorenz, K. Electrical characterization of molybdenum oxide lamellar crystals irradiated with UV light and proton beams. *Surf. Coat. Technol.* **2018**, *355*, 50–54. [[CrossRef](#)]
13. Zhetbaev, A.; Ibragimov, S.S.; Shokanov, A. Mössbauer study of molybdenum oxidation kinetics. *J. Phys. Colloq.* **1980**, *41*, C1-387–C1-388. [[CrossRef](#)]
14. Qi, B.; Gunnlaugsson, H.P.; Ólafsson, S.; Gislason, H.P.; Thorsteinsson, E.B.; Arnalds, U.B.; Mantovan, R.; Unzueta, I.; Zybkin, D.V.; Bharuth-Ram, K.; et al. Metal-insulator transition in crystalline V₂O₃ thin films probed at atomic scale using emission Mössbauer spectroscopy. *Thin Solid Films* **2020**, *714*, 138389. [[CrossRef](#)]
15. Zybkin, D.V.; Gunnlaugsson, H.P.; Gonçalves, J.N.; Bharuth-Ram, K.; Qi, B.; Unzueta, I.; Naidoo, D.; Mantovan, R.; Masenda, H.; Ólafsson, S.; et al. Experimental and theoretical study of electronic and hyperfine properties of hydrogenated anatase (TiO₂): Defect interplay and thermal stability. *J. Phys. Chem. C* **2020**, *124*, 7511–7522. [[CrossRef](#)]
16. Stevens, J.G. Isomer shift reference scales. *Hyperfine Interact.* **1983**, *13*, 221–236. [[CrossRef](#)]
17. Peelaers, H.; Chabinyk, M.L.; Van de Walle, C.G. Controlling n-type doping in MoO₃. *Chem. Mater.* **2017**, *29*, 2563–2567. [[CrossRef](#)]
18. Ouyang, Q.-Y.; Li, L.; Wang, Q.-S.; Zhang, Y.; Wang, T.-S.; Meng, F.-N.; Chen, Y.-J.; Gao, P. Facile synthesis and enhanced H₂S sensing performances of Fe-doped α-MoO₃ micro-structures. *Sens. Actuators B Chem.* **2012**, *169*, 17–25. [[CrossRef](#)]
19. Tiwari, S.; Master, R.; Choudhary, R.J.; Phase, D.M.; Ahuja, B.L. Effect of oxygen partial pressure and Fe doping on growth and properties of metallic and insulating molybdenum oxide thin films. *J. Appl. Phys.* **2012**, *111*, 083905. [[CrossRef](#)]
20. Weyer, G.; The ISOLDE Collaboration. Mössbauer spectroscopy at ISOLDE. *Hyperfine Interact.* **2000**, *129*, 371–390. [[CrossRef](#)]
21. Weyer, G. Defects in semiconductors—results from Mössbauer spectroscopy. *Hyperfine Interact.* **2007**, *177*, 1–13. [[CrossRef](#)]
22. Johnston, K.; Schell, J.; Correia, J.G.; Deicher, M.; Gunnlaugsson, H.P.; Fenta, A.S.; David-Bosne, E.; Costa, A.R.G.; Lupascu, D.C. The solid state physics programme at ISOLDE: Recent developments and perspectives. *J. Phys. G Nucl. Part. Phys.* **2017**, *44*, 104001. [[CrossRef](#)]
23. Catherall, R.; Andreazza, W.; Breitenfeldt, M.; Dorsival, A.; Focker, G.J.; Gharsa, T.P.; Giles, T.; Grenard, J.-L.; Locci, F.; Martins, P.; et al. The ISOLDE facility. *J. Phys. G Nucl. Part. Phys.* **2017**, *44*, 094002. [[CrossRef](#)]
24. Mantovan, R.; Fallica, R.; Gerami, A.M.; Mølholt, T.E.; Wiemer, C.; Longo, M.; Gunnlaugsson, H.P.; Johnston, K.; Masenda, H.; Naidoo, D.; et al. Atomic-scale study of the amorphous-to-crystalline phase transition mechanism in GeTe thin films. *Sci. Rep.* **2017**, *7*, 8234. [[CrossRef](#)] [[PubMed](#)]
25. Ziegler, J.F.; Ziegler, M.D.; Biersack, J.P. SRIM—The Stopping and Range of Ions in Matter. *Nucl. Instr. Meth.* **2010**, *B268*, 1818–1823. [[CrossRef](#)]
26. Kresse, G.; Furthmüller, J. Efficient iterative schemes for ab initio total-energy calculations using a plane-wave basis set. *Phys. Rev. B* **1996**, *54*, 11169–11186. [[CrossRef](#)]
27. Blöchl, P.E. Projector augmented-wave method. *Phys. Rev. B* **1994**, *50*, 17953–17979. [[CrossRef](#)]
28. Perdew, J.P.; Burke, K.; Ernzerhof, M. Generalized gradient approximation made simple. *Phys. Rev. Lett.* **1996**, *77*, 3865–3868. [[CrossRef](#)]
29. Dudarev, S.L.; Botton, G.A.; Savrasov, S.Y.; Humphreys, C.J.; Sutton, A.P. Electron-energy-loss spectra and the structural stability of nickel oxide: An LSDA + *U* study. *Phys. Rev. B* **1998**, *57*, 1505–1509. [[CrossRef](#)]
30. Zheng, H.C. Vapour phase growth of orthorhombic molybdenum trioxide crystals at normal pressure of purified air. *J. Cryst. Growth* **1998**, *186*, 393–402. [[CrossRef](#)]
31. Py, M.A.; Maschke, K. Intra- and interlayer contributions to the lattice vibrations in MoO₃. *Physica B+C* **1981**, *105*, 370–374. [[CrossRef](#)]
32. Dieterle, M.; Weinberg, G.; Mestl, G. Raman spectroscopy of molybdenum oxides: Part I. Structural characterization of oxygen defects in MoO_{3-x} by DR UV/VIS, Raman spectroscopy and x-ray diffraction. *Phys. Chem. Chem. Phys.* **2002**, *4*, 812–821. [[CrossRef](#)]
33. Vila, M.; Díaz-Guerra, C.; Lorenz, K.; Piqueras, J.; Piš, I.; Magnano, E.; Munuera, C.; Alves, E.; García-Hernández, M. Effects of thermal annealing on the structural and electronic properties of rare earth-implanted MoO₃ nanoplates. *CrystEngComm* **2017**, *19*, 2339–2348. [[CrossRef](#)]
34. Mølholt, T.E.; Gunnlaugsson, H.P.; Johnston, K.; Mantovan, R.; Masenda, H.; Ólafsson, S.; Bharuth-Ram, K.; Gislason, H.P.; Langouche, G.; Weyer, G. ISOLDE Collaboration. Spin-lattice relaxations of paramagnetic Fe³⁺ in ZnO. *Phys. Scr.* **2012**, *2012*, 014006. [[CrossRef](#)]
35. Mølholt, T.E.; Mantovan, R.; Gunnlaugsson, H.P.; Naidoo, D.; Ólafsson, S.; Bharuth-Ram, K.; Fanciulli, M.; Johnston, K.; Kobayashi, Y.; Langouche, G.; et al. Observation of spin-lattice relaxations of dilute Fe³⁺ in MgO by Mössbauer spectroscopy. *Hyperfine Interact.* **2010**, *197*, 89–94. [[CrossRef](#)]
36. Gunnlaugsson, H.P. A simple model to extract hyperfine interaction distributions from Mössbauer spectra. *Hyperfine Interact.* **2006**, *167*, 851–854. [[CrossRef](#)]
37. Gunnlaugsson, H.P. Spreadsheet based analysis of Mössbauer spectra. *Hyperfine Interact.* **2016**, *237*, 79. [[CrossRef](#)]
38. Gütllich, P.; Bill, E.; Trautwein, A.X. *Mössbauer Spectroscopy and Transition Metal Chemistry: Fundamentals and Applications*; Springer: Berlin/Heidelberg, Germany, 2011.

39. Sitepu, H.; O'Connor, B.H.; Li, D. Comparative evaluation of the march and generalized spherical harmonic preferred orientation models using X-ray diffraction data for molybdate and calcite powders. *J. Appl. Crystallogr.* **2005**, *38*, 158–167. [[CrossRef](#)]
40. Momma, K.; Izumi, F. VESTA 3 for three-dimensional visualization of crystal, volumetric and morphology data. *J. Appl. Crystallogr.* **2011**, *44*, 1272–1276. [[CrossRef](#)]
41. Ma, W.; Alonso-González, P.; Li, S.; Nikitin, A.Y.; Yuan, J.; Martín-Sánchez, J.; Taboada-Gutiérrez, J.; Amenabar, I.; Li, P.; Vélez, S.; et al. In-plane anisotropic and ultra-low-loss polaritons in a natural van der Waals crystal. *Nature* **2018**, *562*, 557–563. [[CrossRef](#)]
42. Greenwood, N.N.; Gibb, T.C. *Mössbauer Spectroscopy*; Chapman and Hall: London, UK, 1971.
43. Wdowik, U.D.; Ruebenbauer, K. Calibration of the isomer shift for the 14.4-keV transition in ⁵⁷Fe using the full-potential linearized augmented plane-wave method. *Phys. Rev. B* **2007**, *76*, 155118-1–155118-6. [[CrossRef](#)]
44. Blaha, P.; Schwarz, K.; Tran, F.; Laskowski, R.; Madsen, G.K.H.; Marks, L.D. WIEN2k: An APW+lo program for calculating the properties of solids. *J. Chem. Phys.* **2020**, *152*, 074101. [[CrossRef](#)] [[PubMed](#)]
45. Car, R.; Parrinello, M. Unified approach for molecular dynamics and density-functional theory. *Phys. Rev. Lett.* **1985**, *55*, 2471–2474. [[CrossRef](#)] [[PubMed](#)]
46. Gunnlaugsson, H.P.; Mantovan, R.; Masenda, H.; Mølholt, T.E.; Johnston, K.; Bharuth-Ram, K.; Gíslason, H.; Langouche, G.; Naidoo, D.; Ólafsson, S.; et al. ISOLDE Collaboration. Defect annealing in Mn/Fe-implanted TiO₂ (rutile). *J. Phys. D Appl. Phys.* **2014**, *47*, 065501-1–065501-7. [[CrossRef](#)]
47. Gunnlaugsson, H.P.; Johnston, K.; Mølholt, T.E.; Weyer, G.; Mantovan, R.; Masenda, H.; Naidoo, D.; Ólafsson, S.; Bharuth-Ram, K.; Gíslason, H.P.; et al. ISOLDE Collaboration. Lattice locations and properties of Fe in Co/Fe co-implanted ZnO. *Appl. Phys. Lett.* **2012**, *100*, 042109-1–042109-4. [[CrossRef](#)]
48. Schell, J.; Correia, J.G.M.; Lorenz, K.; Peres, M.; Díaz-Guerra, C.; Gunnlaugsson, H.P.; Tarazaga, A.; Deicher, M. Study of Molybdenum Oxide by Means of Perturbed Angular Correlations and Mössbauer Spectroscopy. Proposal to the ISOLDE and Neutron Time-of-Flight Committee. 2016, CERN-INTC-2016-004/INTC-P-454. Available online: <https://cds.cern.ch/record/2119980/files/INTC-P-454.pdf> (accessed on 31 May 2022).